A High-Power MEMS Electric Induction Motor

Carol Livermore, *Member, IEEE*, Anthony R. Forte, Theodore Lyszczarz, *Member, IEEE*,
Stephen D. Umans, *Fellow, IEEE*, Arturo A. Ayon, *Senior Member, IEEE*, and Jeffrey H. Lang, *Fellow, IEEE*

Abstract—An electric induction micromotor with a 4-mm-diameter rotor was designed and built for high-power operation. Operated at partial actuating voltage, the motor has demonstrated an air gap power in excess of 20 mW and torque of $3.5~\mu\mathrm{N\,m}$ at speeds in excess of 55 000 rpm. Operation at higher power and speed was limited by bearing stability at higher rotational speeds. The device builds on an earlier micromotor demonstrated by Frechette *et al.* The high power of the present motor is enabled by its low-loss, high-voltage electric stator, which also offers improved efficiency. The development of this electromechanical device is an important enabling step not only for watt-scale micromotors, but also for the development of microelectric generators. This paper presents the motor's design, the fabrication process that was created to meet its stringent design requirements, and its performance to date.

[1131]

Index Terms—Electric induction, microfabrication, micromotor, power microelectromechanical systems (MEMS).

I. INTRODUCTION

APPLICATIONS for Power MEMS range from generating portable electric power, to propelling microscale vehicles, to driving miniature devices like pumps or fans. However, the substantial power handling potential of such devices is accompanied by substantial challenges in their development. High power also implies high levels of other characteristics, such as voltages, currents, temperatures, frequencies, and/or speeds.

A team at the Massachusetts Institute of Technology (MIT) is developing a family of Power MEMS devices for applications like those described above [2]. The device described here is an electric induction micromotor designed to convert electric power into mechanical power at the watt level. To function at these power levels, the motor is designed to operate at high volt-
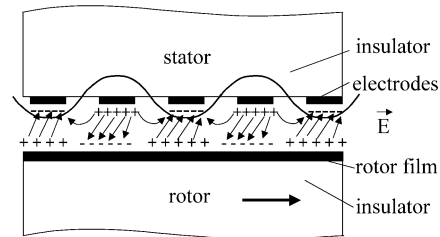
Fig. 1. Schematic diagram of electric induction motor operation. A traveling wave of potential on the stator electrodes induces image charges in the rotor film; the resulting tangential electric field spins the rotor.

ages (about 300 V), high electric frequencies (a few megahertz), and high rotational speeds (greater than 1 Mrpm). These same design requirements, coupled with low electric losses, would enable a microscale electric generator. The purpose of this paper is to demonstrate that a microscale machine can be designed and fabricated to meet these specifications, and to characterize its performance over a range of operating conditions. We are aware of no other groups that are developing electric induction micromotors.

II. DEVICE DESIGN

The motor's actuating principle is electric induction, which is illustrated in Fig. 1. The motor has two fundamental components, a spinning rotor disk and a fixed stator. Covering the stator surface is an array of radial electrodes, arranged like spokes on a wheel, which are excited with ac voltages to create a traveling wave of potential around the stator surface. Facing the stator is the spinning rotor, which is coated with a thin film of a slightly conducting material. The stator and rotor are separated by a 3-μm air gap. The electric potential on the stator induces image charges on the rotor film. As the stator excitation travels along, the image charges follow, conducting through the rotor film. By design, the conductivity of the rotor film is low enough that the rotor charges lag behind the stator excitation. This generates a tangential electric field that pulls on the rotor charges to create a torque, thereby converting electric power into mechanical power. In generator mode, an external source of mechanical power spins the rotor at a speed greater than the traveling speed of the stator excitation. The tangential component of electric field in the gap is reversed, slowing the rotor and sourcing electric power into the stator. Further description and models of electric induction machines may be found in [3]–[5]. A microscale electric induction motor has the potential to operate at higher power density than would a macroscale electric induction machine because the small gap between rotor and stator can sustain higher electric fields without electric breakdown than could a larger gap [6].
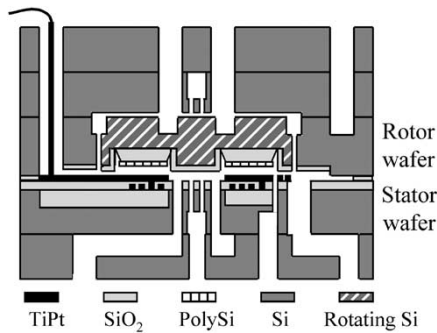
Fig. 2. Cross-sectional schematic diagram of motor showing its five constituent through-etched wafers. Also shown is the integration of the electrical stator and rotor into the stack.

Fig. 3. Fabricated die levels of the micromotor. The electric stator is second from the left, and both sides of the rotor are shown below.

The motor's rotor and stator are integrated into a micromachined static silicon structure. The complete motor comprises a stack of five silicon wafers; a schematic cross section of the device is shown in Fig. 2. Two of the wafers are patterned with thick and thin films of up to 20-μm thickness to create the motor's electric stator and electric rotor. The electric stator is a planar array of 786 radial electrodes grouped into six phases by a separate layer of interconnections, forming 131 pole pairs. On the side of the rotor that faces the stator, the spinning rotor disk is covered by a 0.5-μm-thick layer of moderately (5×10^{12} cm^{-2}) boron-doped polysilicon, which serves as the rotor film. The back side supports a set of turbine blades; these can be driven with compressed air to characterize the rotational performance of the device in the absence of electric excitation. In related applications, blades could form the working part of a compressor or pump, or turbine blades could drive rotation of the disk for electric power generation. The wafers are deep-etched to define the freely moving, 4.2-mm diameter, 550-μm-thick rotor, along with its system of supporting gas bearings and auxiliary fluid systems. In operation, the rotor is supported both axially and in-plane on films of externally pressurized air that are injected into narrow gaps between the rotating and stationary components. Such bearings have previously been demonstrated to support rotation of a similar microdevice at speeds well over 1 Mrpm [7].

Achieving high-power, low-loss motor performance depends on maximizing the capacity to convert electric power to mechanical power and maximizing efficiency. Analytical system modeling was used to examine the tradeoffs among operating point, conversion capacity, ease of fabrication, and losses in the device and electronics. The results show that minimizing stray capacitance between the electric components and the substrate is critical for both power conversion capacity and the minimization of electric losses. To meet this requirement, the design calls for insulating layers that are tens of micrometers thick. The thick insulators reduce parasitic capacitance, which in turn minimizes power dissipation as the parasitic capacitance is charged and discharged through the device's series resistance. However, depositing and patterning such thick films complicates fabrication and makes wafer bonding more difficult. Second, modeling shows that it is imperative to be able to sustain high electric fields of about 10^8 V/m at high frequencies between components separated by several micrometers without suffering elec-
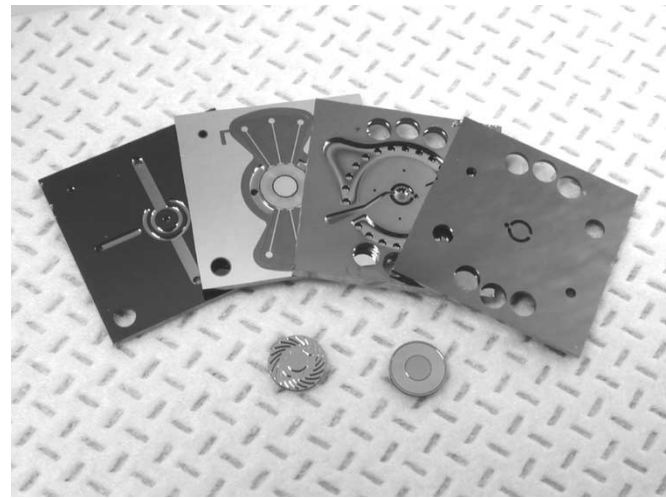
tric breakdown. The higher design frequencies enable higher power, and output power increases as the square of the operating voltage. However, high voltage demands cleanliness and smooth line edges on the electric stator; defects contribute to early failure from electric breakdown. In addition, the electrodes and interconnects must be fabricated of a low-resistivity metal to minimize resistive electric losses. This requirement must be balanced against the thermal and chemical stability that the microfabrication process demands.

III. FABRICATION

The rotor and fluid flow paths are defined in the device's five constituent silicon wafers by double-sided, aligned deep-reactive ion etching (DRIE). This portion of the fabrication is similar to the process described in [7]. Fig. 3 shows a photograph of dies from each of the five wafer levels; only four dies are visible because two of the levels are already bonded together. The device is designed to use wafer-scale fusion bonding for the final assembly. However, the device described here was instead assembled at the die level by clamping the individual dies together in an aluminum/acrylic package. The o-rings that create sealed fluidic connections between the outer ports of the device and the inner surface of the package also provide compression to minimize leakage between plates. This provides an experimental advantage: the device can be disassembled for inspection, cleaning, or to perform diagnostics.

The design requirements of low losses and high electric fields primarily impact the fabrication of the electric rotor and the electric stator. While the rotor fabrication process is similar to that used in [1], the stator fabrication process is significantly different. For this reason, the emphasis here will be on the stator fabrication process.

Both the stator and rotor are fabricated on 10- to 20-μm-thick silicon dioxide layers to minimize stray capacitance of their electric elements to the substrate. To minimize wafer bow while maintaining a planar wafer surface, the thick oxide layers are limited to isolated oxide islands that are embedded in the silicon substrate. A cross section of an embedded oxide island in
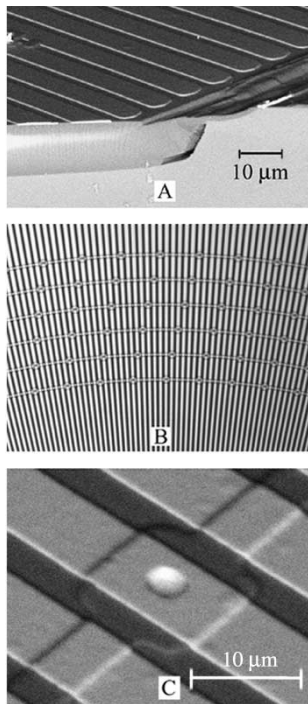
Fig. 4. (a) SEM of stator cross section, showing electrodes on a recessed oxide island. (b) Optical micrograph of the stator structure, showing electrodes grouped by interconnection rings. (c) SEM of electrodes and interconnection ring, connected by an electrical via.
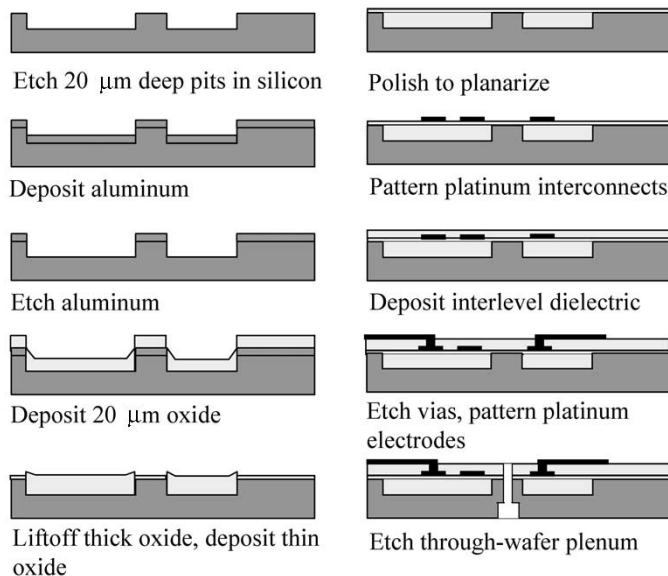

Fig. 5. Schematic cross-sectional fabrication process flow for the stator wafer.

the stator is shown in Fig. 4(a). The island concept has been demonstrated previously [8], but in the present stator, the islands are fabricated by a different and direct technique. Thick oxides are deposited in etched recesses in a silicon substrate using a liftoff process, producing a nearly planar oxide surface.

Fig. 5 is a schematic diagram of the stator fabrication process flow. First, 20-μm-deep pits are etched in the silicon substrate. An aluminum layer with micrometer-scale thickness is deposited and then patterned to cover the upper silicon surface but not inside the pits; this serves as the sacrificial layer for the liftoff step. Next, 20 μm of TEOS oxide is deposited over

the wafer surface. Liftoff is accomplished by a prolonged HCl etch; the field oxide breaks off neatly, leaving micrometer-scale stubs at the pit edges. If necessary, the stubs may then be minimized by CMP.

The stator electrodes and interconnection rings are fabricated as two interconnected 0.3-μm-thick platinum levels with titanium adhesion layers. The two platinum layers are fabricated by a liftoff process on top of the thick oxide islands in the silicon substrate. The masking material for the liftoff process is a positive Shipley resist (Microposit S1805) with its surface hardened by chlorobenzene treatment. The interconnection rings are deposited first; each of the six rings will later connect to one of the six phases of the electrodes. A 1-μm-thick layer of TEOS oxide is then deposited over the interconnection rings to provide electrical isolation between the interconnection rings and the electrodes. Next, via holes are etched in the interlayer oxide, and the stator electrodes are deposited with a second platinum liftoff step. Each stator electrode is 900 μm long, tapers from 11 to 4 μm wide, and is separated from its neighboring electrodes by just 4 μm. Via connection between the two layers is made by simple contact between the interconnects and electrodes; no plug fill process is used.

Fig. 4(b) shows the interconnected electrode structure produced by this process, and Fig. 4(c) shows a close-up view of one of the electric vias that connect the two platinum layers. The rounded profile of the via etch visible in Fig. 4(c) enables electrode continuity over the via etch topography. Via resistance is measured at about 3 Ω per contact. This is low enough to enable good performance because each via carries the excitation from an interconnection ring to a single electrode; via resistances do not add up in series. Vias are also used to carry the excitation from the leads to the interconnection rings, but that connection is made by seven parallel vias for each phase.

Platinum was selected for the electrodes and interconnections because it meets three important device requirements. First, platinum's low resistivity, measured at 14 $\mu\Omega$-cm for our films, helps to minimize electric losses in the stator structure. Second, platinum has good thermal and chemical stability. The stator structures are designed to survive temperatures high enough for silicon fusion bonding as well as the organic cleans necessary to prepare the wafer surface for bonding. Third, the very smooth, lifted-off line edges of the platinum features can withstand higher electric fields without electric breakdown than can dry-etched features with rougher edges.

The high temperatures associated with silicon fusion bonding have the potential to damage the platinum electrodes and interconnections that form the motor's electric stator. Agglomeration could impact the continuity and topography of the electrodes and interconnects; those changes could, in turn, impact the electric performance of the device. To limit agglomeration while retaining adequate bond strength, the design incorporates a prolonged lower-temperature wafer-bonding anneal. Candidate bond temperatures in the range from 700 °C to 800 °C were chosen based on previous work that found effective bonding at those temperatures [9]. The thermal budget for the motor's platinum structures was then determined experimentally. Test structures resembling the stator electrodes were fabricated; 0.3-μm-thick platinum features were deposited by a liftoff process over
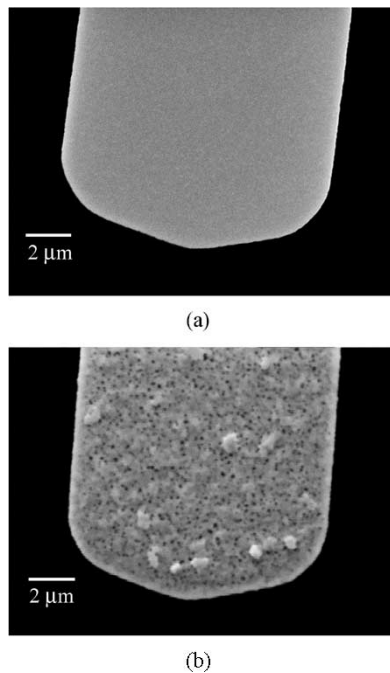
Fig. 6.   SEMs of 0.3-μm-thick platinum, deposited with a titanium adhesion layer on oxide and patterned in the shape of stator electrodes. The sample anneal histories are (a) no anneal after platinum deposition and (b) $800\ °C$ anneal in N_2 for 3 h.
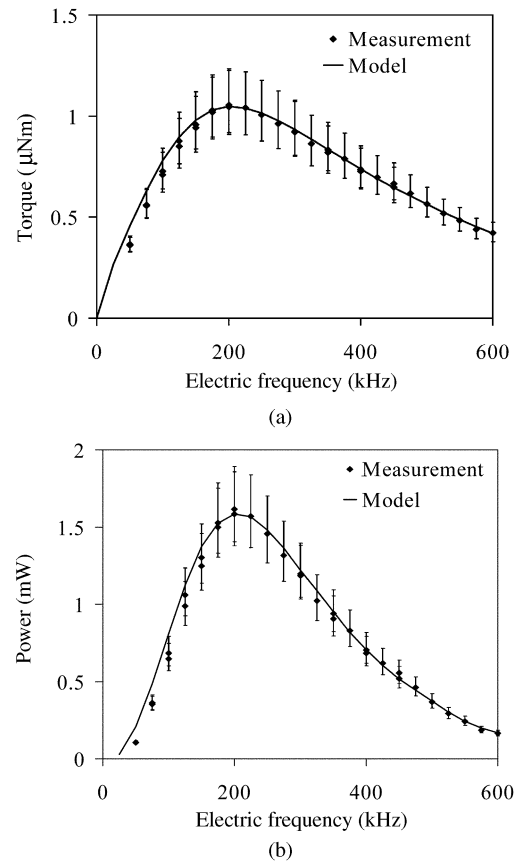

Fig. 7.   (a) Measured motor torque and (b) measured motor power as a function of electrical excitation frequency at a fixed stator excitation voltage of 45 V.

a 100-Angstrom titanium adhesion layer on an oxide-coated silicon wafer. The samples were then annealed in a nitrogen ambient at different temperatures and examined in a scanning electron microscope to identify changes in the film.

Fig. 6 shows SEMs of platinum structures patterned to resemble a stator electrode, both as deposited and after a 3-h anneal at $800\ °C$ in a nitrogen ambient. The duration of anneal was chosen to match the time required to achieve bonding at $800\ °C$. The film retains its continuity after anneal, but the initially smooth film develops small pits and broader raised areas. The edges of the platinum electrodes do not develop pronounced topography like the central part of the structure; the smoother edges are important in preventing breakdown. The width of this edge region is comparable to the film thickness.

The resistance of the interconnected electrode structures to electric breakdown was measured experimentally. A sinusoidal potential difference with an amplitude of up to 300 V and a frequency of 1.75 MHz was applied between neighboring stator electrode phases. This is representative of the stator excitation at the design point. While the voltage was applied, the electrode structure was examined under an optical microscope to identify signs of electrode damage. With defect-free lithography, the electrode structure resisted electric breakdown up to 300 V. However, it is important that the structure be defect-free; debris or other defects between the electrodes can initiate electric breakdown. For debris-mediated breakdown, the breakdown was typically observed to halt after elimination of the initial flaw.

IV. EXPERIMENTAL RESULTS

The motor's performance is characterized as a function of stator excitation voltage and frequency. The hydrostatic gas

bearings are first pressurized to float the rotor on a film of air; the stator is then excited with a traveling wave of electric potential to excite the motor. A fiber optic sensor is inserted into a port in the device to monitor the passage of deep-etched features on the rotor. A spectrum analyzer processes the sensor's output to yield the motor's rotational speed. The motor operates with only viscous load; its speed is set by the balance between its drive torque and the viscous drag on the spinning rotor. The viscous torque is measured as a function of rotational speed. The motor's torque and power are then extracted from the measured rotational speed using the experimentally determined load line.

The motor's load line is measured by abruptly removing the stator excitation and monitoring the rotor's deceleration with the optical speed sensor. From these data and the known rotor inertia, we can extract the decelerating viscous torque. This yields a fixed viscous torque constant of $(5.6 \pm 1) \times 10^{-4}\ \mu\text{N} \cdot \text{m} \cdot \text{s}$ plus a constant $0.2 \pm 0.01\ \mu\text{N} \cdot \text{m}$ component of the torque that likely reflects mechanical rubbing of a piece of debris in the forward thrust bearing. The measured viscous torque constant is higher than would be expected if the rotor were vertically centered in its housing. Instead, the measured value matches the viscous torque constant calculated for a rotor positioned just 0.1 μm from the aft thrust bearing surface.

Fig. 7 plots the motor's torque and power measured as a function of electric frequency for a fixed stator excitation voltage of 45 V_{peak}. The solid lines are fits of a model [3]–[5] to the data,
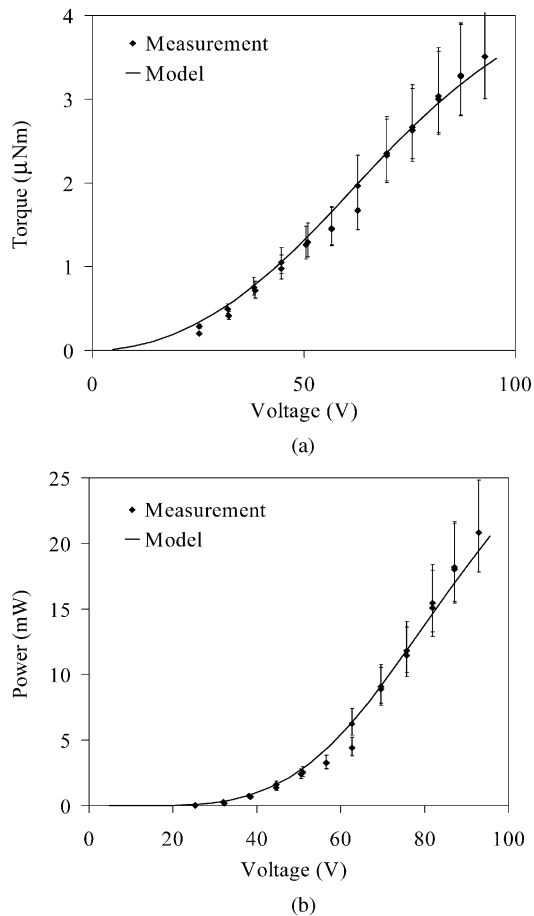
Fig. 8. (a) Measured motor torque and (b) measured motor power as a function of stator excitation voltage at a fixed stator excitation frequency of 200 kHz.

with the rotor film conductivity and motor gap having been adjusted for a best fit. The measured torque and power both peak at about 200 kHz. This peak frequency reflects the resistivity of the moderately doped polysilicon film on the rotor surface, and corresponds to a rotor film sheet conductance of 1.25 nS/square. This is lower than the target conductance of 3 nS/square for this device and likely reflects the omission of high temperature wafer bonding anneals that would promote grain growth in the polysilicon film.

The peak amplitudes of the measured torque and power reflect the gap between the rotor and stator; more power is converted across a smaller air gap. The data correspond to a motor gap of 1.81 μm. This is smaller than the design value of 3 μm, enabling more power. The reduced gap is consistent with the as-fabricated device geometry and the measured viscous torque. The nominally 3 μm motor gap is reduced by the shift of the rotor to the aft side of its housing; a slightly recessed stator structure partially compensates for the shift. Using these values for motor gap and rotor film resistivity, measured and predicted values of torque and power match well.

Fig. 8 plots the motor's torque and power measured as a function of the amplitude of the actuating voltage at the fixed electric frequency of 200 kHz. The torque starts to increase quadratically with voltage, as expected; the trend has an inflection point because the rotor speed cannot exceed the relatively low synchronous speed of the stator excitation at 200 kHz. The max-

imum measured torque is 3.5 μNm at a speed of over 55 000 rpm for an excitation voltage of 95 V_{peak}. The maximum air gap power attained exceeds 20 mW, corresponding to a power density of 35 kW/m^3. The solid line is the device performance calculated from the model using the motor gap and rotor film resistivity determined above. Using the same parameters, the data again agree well with theory.

The motor's electromechanical efficiency may be defined as the ratio of power delivered to the viscous load to total power entering the motor's stator. For the experiments described here, the point of peak power conversion is also the point of peak efficiency. The efficiency at this point is about 61%. Most of the losses are resistive losses in the rotor film. The partial efficiency from rotor film dissipation η_{rotor} is given by

$$\eta_{rotor} = 1 - \frac{m\Omega}{\omega} \qquad (1)$$

where m is the number of pole pairs on the stator, Ω is the angular velocity of rotation, and ω is the angular frequency of the stator excitation. This is the efficiency by which our motor converts electrical air gap power into mechanical shaft power. The experimental values of Ω and ω yield a rotor efficiency of 62%. The small remaining loss comes from resistive losses in the stator conductors and has been modeled. The stator losses reduce the overall efficiency to about 61%.

The maximum actuating voltage in these tests was not limited by electric breakdown, but rather by the high rotational speeds that are necessary to balance a large actuating torque against viscous drag under no-load operating conditions. However, the stators' demonstrated ability to withstand design fields suggests that the motors will be able to attain design voltage and power levels as well.

This micromotor compares well with macro-scale magnetic integral horsepower industrial motors on performance metrics like the shear stress on the rotor and the ratio of this shear stress to the normal force. The maximum shear stress attained so far by our electric motors is about 210 N/m^2, at approximately half of the design electric field. If these results are scaled up to full field, as tests on the electrical stators indicate should be possible, the shear stress would be about 800 N/m^2, as compared with about 7000 N/m^2 for a typical integral horsepower magnetic induction machine [10]. The ratio of shear stress to normal pressure attained in our electric motors so far is about 2%, comparable to the typical magnetic induction machine described above. The micromotor's ability to harness the available energy density in its air gap is comparable to that of a macroscale magnetic machine.

V. CONCLUSION

An electric induction micromotor designed for high-power operation was fabricated. Operated at partial actuating voltage, the motor demonstrated an air gap power in excess of 20 mW and torque of 3.5 μNm at speeds in excess of 55 000 rpm. This was enabled by the development of low-loss, high-voltage electric stators, which have been demonstrated to successfully sustain design voltages in experiments. The electric isolation of stator components from the rest of the device was accomplished

by the incorporation of thick islands of oxide that were embedded in the silicon substrate. These islands were formed by a liftoff technique that enabled automatic and nearly complete planarization of the island oxide with the surrounding silicon surface.

ACKNOWLEDGMENT

REFERENCES

[1] L. G. Frechette, S. F. Nagle, R. Ghodssi, S. D. Umans, M. A. Schmidt, and J. Lang, "An electrostatic induction micromotor supported on gas-lubricated bearings," in *Proc. Tech. Dig. 14th IEEE International Conference on Micro Electro Mechanical Systems*, Interlaken, Switzerland, Jan. 2001, pp. 290–293.

[2] A. H. Epstein *et al.*, "Micro-heat engines, gas turbines, and rocket engines—The MIT microengine project," in *Proc. AIAA Paper 97–1773, 28th AIAA Fluid Dynamics Conference*, Snowmass Village, CO, June–July 29–2, 1997.

[3] S. F. Bart and J. H. Lang, "An analysis of electroquasistatic induction micromotors," *Sens. Actuators*, vol. 20, pp. 97–106, Nov. 1989.

[4] S. F. Nagle, "Analysis, Design, and Fabrication of an Electric Induction Micromotor for a Micro Gas-Turbine Generator," Ph.D. dissertation, Massachusetts Institute of Technology, Cambridge, 2000.

[5] S.F. Nagle, C. Livermore, L.G. Frechette, R. Ghodssi, and J.H. Lang, "A microscale electric induction motor," J. Microelectromech. Syst., submitted for publication.

[6] F. Paschen, "Ueber die zum funkenübergang in luft, wasserstof und kohlensäure bei verschiedenen drucken erforderliche potentialdifferenz," *Annal der Physik*, vol. 37, pp. 69–96, 1889.

[7] L. G. Frechette, S. A. Jacobson, F. F. Ehrich, R. Ghodssi, R. Khanna, C. W. Wong, X. Zhang, K. S. Breuer, M. A. Schmidt, and A. H. Epstein, "Demonstration of a microfabricated high-speed turbine supported on gas bearings," in *Proc. Tech. Dig. 2000 Solid-State Sensor and Actuator Workshop*, Hilton Head Island, SC, June 2000, pp. 43–47.

[8] R. Ghodssi, L. G. Frechette, S. F. Nagle, X. Zhang, A. A. Ayon, S. D. Senturia, and M. A. Schmidt, "Thick buried oxide in silicon (TBOS): An integrated fabrication technology for multi-stack wafer-bonded MEMS processes," in *Proc. 10th Int. Conf. Solid-State Sensors*, Sendai, Japan, June 1999.

[9] A. A. Ayon, X. Zhang, K. T. Turner, D. Choi, B. Miller, S. F. Nagle, and S. M. Spearing, "Characterization of silicon wafer bonding for power MEMS applications," *Sens. Actuators, Phys. A*, vol. 103, pp. 1–8, January 2003.

[10] T. J. E. Miller, *Switched-Reluctance Motors and Their Control*. Oxford, U.K.: Oxford University Press, 1993.

Anthony R. Forte, deceased, received the Associate's degree in computer engineering from Franklin Institute, Boston, MA, in 1980.

In the same year, he joined the Lincoln Laboratory with the Microelectronics Group, Lexington, MA, working primarily toward the development of dry-etched processes for metals. Some additional responsibilities included the development of noncrystallographic dry-etch processes for GaAs, as well as high-aspect-ratio dry etching of silicon for permeable base transistors. In 1988, he joined the Submicrometer Technology Group at Lincoln Laboratory. There, he developed plasma-deposited electrochromic thin films for use in 193-nm lithography, silylation processes for top-surface imaging and the corresponding dry-etch processes for pattern transfer for 193-nm lithography, and power MEMS devices.

Theodore Lyszczarz (S'73–M'79) received the Ph.D. degree in electrical engineering and computer science from the Massachusetts Institute of Technology (MIT), Cambridge, in 1979.

Since graduation, he has worked in the Solid State Division at the MIT Lincoln Laboratory. He has worked on high-resolution alignment techniques for optical lithography, and has fabricated advanced GaAs and silicon devices using electron beam lithography. In 1991, he was named the Assistant Group Leader of the Submicrometer Technology Group at Lincoln Laboratory. Since then, he has worked on metrology issues, field emission cathodes, and microfabrication techniques.

Stephen D. Umans (S'67–M'75–SM'82–F'95) received the S.B. and S.M. in electrical engineering from the Massachusetts Institute of Technology (MIT), Cambridge, in 1972 and 1976, respectively.

He is Principal Research Engineer in the Electromechanical Systems Laboratory and the Electrical Engineering and Computer Science Department at MIT. He is coauthor of the textbook *Electric Machinery* (New York: McGraw-Hill). His research interests include electromechanics, electric power systems and both macro- and microscale electric machinery.

Arturo A. Ayon (S'93–M'95–SM'00) received the Ph.D. degree in nuclear science and engineering from Cornell University, Ithaca, NY, in 1996.

In 1983, he joined the IBM Computer Manufacturing Facility, Guadalajara, Mexico, as a Manufacturing Engineer. In the same year, he moved to Rochester, MN, to serve as Liaison Engineer between the IBM manufacturing plant in Mexico and the IBM development plant in United States. In 1985, he was appointed Manufacturing and Quality Engineering Manager and returned to Mexico to oversee the operation of the newly installed manufacturing lines for IBM computer systems. In 1986, he opened a marketing and distribution center for plastic commodities in Guadalajara, Mexico. Later, he sold that operation to return to graduate school to Cornell University. Between 1996 and 2000, he was a Research Scientist at the Massachusetts Institute of Technology, Cambridge, MA. He was involved in the development and fabrication of microturbomachinery, power generation microdevices, inertial sensors and thin-film characterization. In 2000, he joined Sony Semiconductor heading the MEMS Business Development group to initiate, coordinate, and oversee the involvement of Sony San Antonio in the emerging MEMS markets and to promote the application of MEMS technology to Sony products. His interests include deep-reactive ion etching, wafer bonding, low-k dielectrics, actuators, thin-film properties, and the application of MEMS technology to RF, optics, and power generation.

Dr. Ayón is a Member of the American Vacuum Society, the Electrochemical Society, the IEEE Electron Devices Society, and the Materials Research Society.

Carol Livermore (M'99) received the B.S. degree in physics from the University of Massachusetts, Amherst, in 1993 and the A.M. and Ph.D. degrees in physics from Harvard University, Cambridge, in 1995 and 1998, respectively.

From 1998 to 2002, she was first a Postdoctoral Associate and then a Research Scientist at the Massachusetts Institute of Technology (MIT), Cambridge. Currently, she is an Assistant Professor in the Department of Mechanical Engineering at MIT. Her research interests include power MEMS and the development of techniques and applications for nano- and microscale self-assembly.

Jeffrey H. Lang (S'78–M'79–SM'95–F'98) received the S.B., S.M., and Ph.D. degrees in electrical engineering from the Massachusetts Institute of Technology (MIT), Cambridge, in 1975, 1977, and 1980, respectively.

Currently, he is a Professor of Electrical Engineering at MIT and has been a faculty member since 1980. His research and teaching interests focus on the analysis, design, and control of electromechanical systems with an emphasis on rotating machinery, microsensors and actuators, and flexible structures. He has written over 160 papers and holds 10 patents in the areas of electromechanics, power electronics and applied control, and has been awarded four best paper prizes from various IEEE societies.

Prof. Lang is a former Hertz Foundation Fellow and a former Associate Editor of *Sensors and Actuators*.